Journal of Instrumentation

PAPER

IsoDAR@Yemilab: A report on the technology, capabilities, and deployment

To cite this article: J.R. Alonso *et al* 2022 *JINST* **17** P09042

Published by IOP Publishing for Sissa Medialab

Received: *February 23, 2022*
Revised: *June 30, 2022*
Accepted: *August 8, 2022*
Published: *September 28, 2022*

IsoDAR@Yemilab: A report on the technology, capabilities, and deployment

J.R. Alonso,[a,*] J.M. Conrad,[a] D. Winklehner,[a,*] J. Spitz,[d] L. Bartoszek,[h] A. Adelmann,[f] K.M. Bang,[i] R. Barlow,[c] A. Bungau,[a] L. Calabretta,[e] Y.D. Kim,[i] D. Mishins,[d] K.S. Park,[i] S.H. Seo,[i] M. Shaevitz,[b] E.A. Voirin[j] and L.H. Waites[a]

[a] *Department of Physics, Massachusetts Institute of Technology, 77 Massachusetts Ave, Cambridge, U.S.A.*
[b] *Department of Physics, Columbia University, 538 West 120th Street, New York, U.S.A.*
[c] *School of Computing and Engineering, University of Huddersfield, Queensgate, Huddersfield, U.K.*
[d] *Department of Physics, University of Michigan, 450 Church Street, Ann Arbor,U.S.A.*
[e] *INFN Laboratori Nazionali di Legnaro, Viale dell'Università, Legnaro, Italy*
[f] *Paul Scherrer Institute, Forschungsstrasse 111, Villigen PSI, Switzerland*
[h] *Bartoszek Engineering, 818 W. Downer Place, Aurora, U.S.A.*
[i] *Center for Underground Physics, Institute for Basic Science, 55 Expo-ro, Daejon, South Korea*
[j] *eVoirin Engineering Consulting, 2624 Mc Duffee Circle, North Aurora, U.S.A.*

E-mail: JRAlonso@mit.edu, winklehn@mit.edu

Abstract: IsoDAR@Yemilab is a novel isotope-decay-at-rest experiment that has preliminary approval to run at the Yemi underground laboratory (Yemilab) in Jeongseon-gun, South Korea. Here, we describe in detail the considerations for installing this compact particle accelerator and neutrino target system at the Yemilab underground facility. Specifically, we describe the caverns being prepared for IsoDAR, and address installation, shielding, and utilities requirements. To give context and for completeness, we also briefly describe the physics opportunities of the IsoDAR neutrino source when paired with the Liquid Scintillator Counter (LSC) at Yemilab, and review the technical design of the neutrino source.

*Corresponding author.

https://doi.org/10.1088/1748-0221/17/09/P09042

2022 JINST 17 P09042

KEYWORDS: Accelerator Subsystems and Technologies; Models and simulations; Overall mechanics design (support structures and materials, vibration analysis etc); Targets (spallation source targets, radioisotope production, neutrino and muon sources)

ARXIV EPRINT: 2201.10040

2022 JINST 17 P09042

Contents

2022 JINST 17 P09042

1 Introduction

The IsoDAR (Isotope Decay At Rest) source offers a pure $\bar{\nu}_e$ flux from decay of ^{8}Li that, when paired with the Liquid Scintillator Counter (LSC) detector at Yemilab [1], will make precise and definitive measurements of the oscillations due to sterile neutrinos [2] and test for many possible interactions beyond the Standard Model [3], via the inverse β-decay (IBD) $\bar{\nu}_e + p \rightarrow e^+ + n$, and $\bar{\nu}_e$-e^- elastic scattering (ES) processes.

The source makes use of a cyclotron-accelerated beam, delivered to a novel decay-at-rest target-system, producing an isotropic flux of $\bar{\nu}_e$ from the β-decay of 839-millisecond ^{8}Li. The system is described in detail below.

1.1 The structure of this paper

This paper is one of several articles about the IsoDAR experiment and its implementation at the Yemilab underground facility. We first review the physics opportunities in section 1.2, then discuss the required technology in section 1.3 and then the technological advances in the accelerator and the target, in section 2.

The main part of this manuscript is a condensed version of our recent whitepaper: *IsoDAR@Yemilab: A Conceptual Design Report for the Deployment of the Isotope Decay-At-Rest Experiment in Korea's New Underground Laboratory, Yemilab* [4] referred to below as the CDR. As such, it provides a technical review of the requirements and plans for installation at the Yemilab site, making these aspects available for an interested general audience. Further discussion on transport of equipment to the laboratory, handling of equipment underground, consideration of environmental and safety issues and specifications of utilities can be found in the CDR.

1.2 Physics drivers for IsoDAR@Yemilab

Our companion article *Neutrino Physics Opportunities with the IsoDAR Source at Yemilab* [5] gives a detailed description of the neutrino physics program. The physics capabilities are based on the parameters in table 1. The primary IsoDAR physics program is made possible by the unique, single-isotope-produced (^{8}Li$\rightarrow^8$Be$+e^- + \overline{\nu}_e$), the relatively high energy ($< E_{\overline{\nu}_e} > \sim 6$ MeV), and the pure $\bar{\nu}_e$ flux shown in figure 1. The immense (but isotropic) flux of antineutrinos (1.15×10^{23} in 4 years) that is produced in the target assembly, when placed as close as shielding will allow to the LSC, will provide very high statistics: 1.7×10^6 IBD events and 7000 ES events, after cuts.

The neutrino physics measurements with IsoDAR@Yemilab, afforded by the expected high event rate, can be broken up into two categories: (1) a study of any oscillation-like behavior, possibly associated with one or more sterile neutrinos, which would present as a "wave-like" IBD signal in terms of distance traveled (L), energy (E), and/or L/E and (2) a search for non-standard neutrino interactions, which would present as a measured deviation from the well-predicted ES cross section.

Table 1. Assumptions for the physics case. "Cuts" include fiducial volume and cosmic veto timing selection criteria. For ES, this also includes a visible energy requirement $E_{\rm vis} > 3$ MeV. See ref. [5] for more information.

Runtime	5 calendar years
IsoDAR duty factor	80%
Protons on target/year	1.97×10^{24}
^{8}Li/proton ($\overline{\nu}_e$/proton)	0.0146
$\overline{\nu}_e$/ 4 years	1.15×10^{23}
1σ uncertainty in $\overline{\nu}_e$ creation point	0.41 m
IsoDAR@Yemilab mid-baseline	17 m
IsoDAR@Yemilab baseline range	9.5–25.6 m
IsoDAR@Yemilab LS mass	2.26 ktons
IsoDAR@Yemilab LS size (rad, height)	7.5 m, 15.0 m
$\bar{\nu}_e + p \rightarrow e^+ + n$ (IBD)	1.7×10^6 events afer cuts
$\bar{\nu}_e + e^- \rightarrow \bar{\nu}_e + e^-$(ES)	7000 events after cuts

2022 JINST 17 P09042

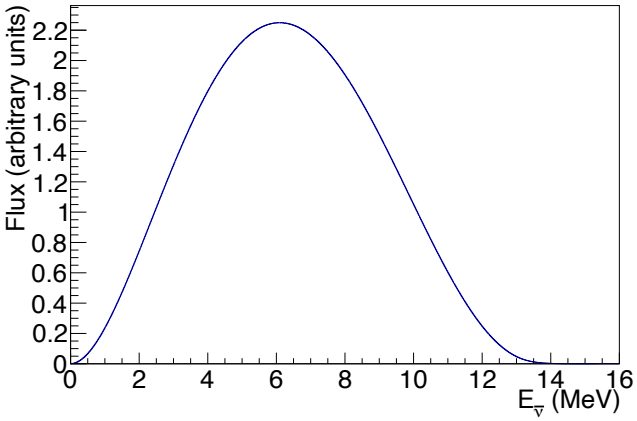

Figure 1. From [5]. The antineutrino energy spectrum from the IsoDAR source.

Both of these physics opportunities are very well motivated, e.g., by the 3–5σ anomalies indicating sterile neutrinos reported in numerous neutrino experiments [6–17] and the simultaneous dearth of data in neutrino-based electroweak scattering [18] and sensitivity to new physics in this sector.

The IsoDAR@Yemilab oscillation search will take advantage of the high rate, low background, and strong energy/vertex detector resolution for gaining unprecedented sensitivity to this new physics. The event rate as a function of L/E for a few example oscillation signatures, including statistical uncertainties and smearing according to the expected energy and vertex resolutions, are shown in figure 2. The figure depicts oscillations in representative 3 + 1 (left), 3 + 2 (middle), and 3 + 1+decay (right) scenarios. The associated sensitivity within a 3 + 1 model is shown in figure 3 [5]. As can be seen, IsoDAR@Yemilab would comfortably provide world-leading sensitivity to oscillations involving a sterile neutrino.

Similarly to the IBD measurement, the IsoDAR@Yemilab ES study will take advantage of high rate, low background, and strong energy/vertex detector resolution in searching for this signature. Figure 4 shows the expected ES signal rate and backgrounds, coming from solar neutrinos, radiogenics, and cosmogenics. In terms of a weak mixing angle measurement, which can be thought of alternatively as the "absence of non-standard neutrino interactions", we expect a $\delta \sin^2 \theta_W$ sensitivity of 1.9%,

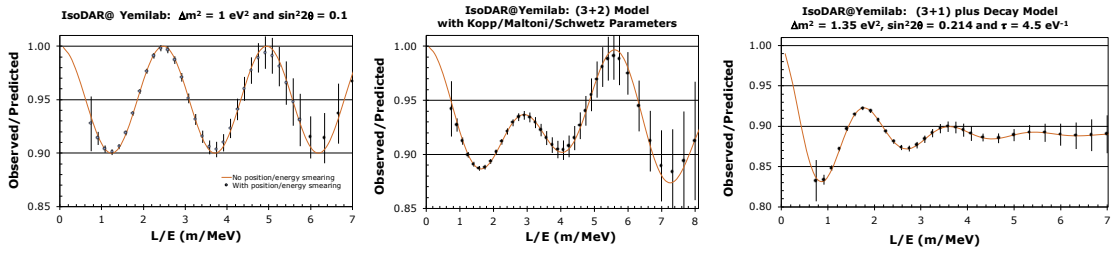

Figure 2. From [5]. The IsoDAR@Yemilab ability to measure oscillations under three example new physics scenarios: a 3 + 1 model (left), a 3 + 2 model (middle), and a 3 + 1+decay model consistent with the 95% allowed region observed at IceCube (right) [19].

2022 JINST 17 P09042

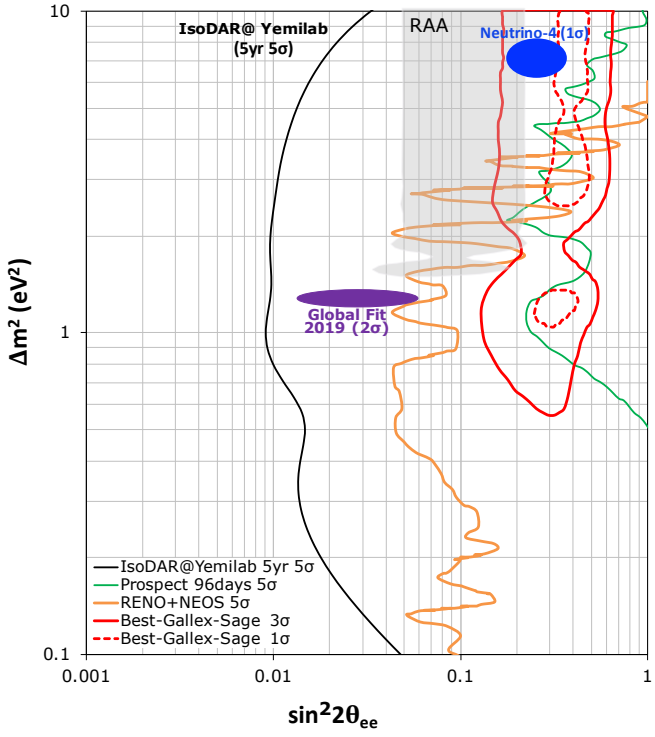

Figure 3. From [5]. The 5σ sensitivity of the IsoDAR@Yemilab experiment after 5 years of running.

using rate and energy-shape information and including statistical and systematic uncertainties, after 5 years of running. With the possible addition of directional reconstruction capabilities in the detector for mitigating signal/electron-like background, we can expect a sensitivity of 1.5% [5]. This can be compared to the current reactor-based global fit of $\sin^2\theta_W = 0.252 \pm 0.030$, a 12% measurement [18].

While the antineutrino flux provides the basis of the main physics IsoDAR@Yemilab program, interactions in the IsoDAR source also produce a high rate of neutrons and photons that are contained within the source region. These can be used for new physics searches involving conversion of photons and neutrons to non-standard particles. For example, ref. [20] provides examples of dark sector searches using a "neutrons-shining-through-walls" method. In addition, an interesting feature of the photon flux from the IsoDAR source that can be exploited towards gaining sensitivity to axions is the presence of mono-energetic lines from the decay of nuclear excited states near the target.

1.3 Requirements and accelerator technology options

The selection of the accelerator type, and design decisions described below are the result of a careful study of requirements as well as capabilities and limitations of existing accelerator technologies. This study can be found in reference [21]; highlights are summarized here.

The fundamental requirements for the IsoDAR experiment are straightforward: deliver a maximum rate of an optimal $\bar{\nu}_e$ spectrum into the fiducial volume of the LSC with minimum cost and maximum efficiency. A cost-efficient package must be specified, and designed to fit in the underground environment adjacent to the large detector, placing emphasis on compactness, reliability, efficiency, and cost. Each of these points will be elaborated below.

2022 JINST 17 P09042

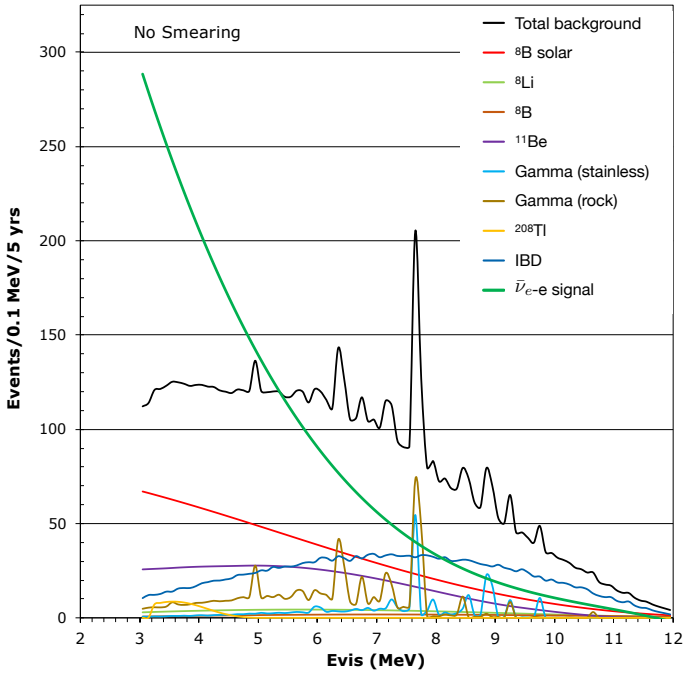

Figure 4. From [5]. The ES signal/background event rates expected after 5 years of running IsoDAR@Yemilab.

- $\bar{\nu}_e$ *spectrum.* To provide a neutrino signal minimally affected by background, the neutrino energies should be above ~4 MeV. Higher energy is also favored due to the increasing interaction cross section. Using ^{8}Li as the parent isotope meets this requirement very well. It provides a clean, well-understood, high-energy spectrum shown in figure 1, with an endpoint close to 14 MeV.

- *Number of Events.* The effectiveness of a neutrino experiment is often ultimately related to the number of events that can be accumulated. For IsoDAR, as the neutrino flux is emitted isotropically around the target, maximizing the number of events is determined by how close the target can be placed to the detector (maximizing the subtended solid angle of the fiducial volume), and by the number of neutrinos produced. Closeness of the target is a careful balance between solid angle and shielding thickness to prevent neutrons produced in the target from penetrating to the fiducial volume. This is discussed in section 3.2.3. The optimum geometry provides about 5% efficiency. The neutrino flux produced from ^{8}Li decays is ultimately related to the number of protons striking the neutron-producing target. Yield calculations have been based on 10 mA of 60 MeV protons striking the target.

  – *Proton energy.* Figure 8 and table 5 of the Cost Effectiveness study [21] address the neutron production for protons striking a target versus energy (result: a straight line on log-log plot; empirically, $[(n/p) \approx 3 \times 10^{-5} \times \mathrm{E}^2]$, where E is in MeV). The obvious conclusion is that higher energies produce substantially more neutrons per proton. Specifically, at 60 MeV the (n/p) ratio is about 0.11, while at 1 GeV the ratio is about 30. But the footprint of a 1 GeV Spallation Source would not fit underground. Figure 10 of [21] addresses the maximum current of different accelerator technologies,

2022 JINST 17 P09042

and clearly shows that isochronous cyclotrons are the most efficient. They can also be compact, making them the clear best choice for an underground installation.

  - *Beam current.* Compact cyclotron designs are very mature, with demonstrated reliability; driven by the medical isotope industry. Current limits for these isotope accelerators are about 1 mA to 2 mA. These limits are driven by beam loss in the central region (at injection energies of a few 10's of keV), and by extraction stripper foil lifetimes due to heating from convoy electrons generated in the stripping of the H^- ions accelerated [22]. As discussed in section 2.1, our technical innovations are expected to allow reaching the 10 mA beam current requirement in a compact cyclotron.

- *Alternate accelerator technologies.* Other than isochronous cyclotrons, compact or separated sector, no other circular accelerator technology could come close to the 10 mA current specification. A separated-sector isochronous-cyclotron based system could undoubtedly be designed using the same features as the compact-cyclotron system being adopted, however the system would be larger.

  A linear accelerator could produce the required peak beam current, but would need to be superconducting to run at the 100% duty factor to achieve the integrated beam power on target. Even if superconducting, a structure to produce 60 MeV protons would be long, the low final energy requiring distributed quarter-wave resonators, so the *engineering* energy gain per meter is low. Fitting such a linac in the Yemilab caverns would be difficult. The cost of such a structure, and added complexity of a cryogenic plant makes such a system unattractive. Ref. [21] concludes the cost would be at least double the cost of a cyclotron system.

The conclusion of our study is that a compact isochronous cyclotron presents the optimal technology to be pursued for the IsoDAR experiment. In the following section we summarize the elements of the system, and progress towards the final design and implementation.

2 Review of the Technical Design and R&D Establishing the IsoDAR Source

The elements of the IsoDAR $\bar{\nu}_e$ source are as follows:

- An ion source producing a $\sim$ 10 mA DC beam of H_2^+ ions.
- A Radio-Frequency Quadrupole (RFQ) buncher that allows $>$ 60% capture of the H_2^+ beam in the cyclotron.
- An axially-injected compact cyclotron that produces an extracted beam of 5 mA of H_2^+ ions at 60 MeV/amu.
- A stripper foil close to the extraction point that converts the 5 mA of H_2^+ to 10 mA of protons, followed by a dipole magnet to direct the stripped protons into the transport line.
- A transport line (MEBT) that brings the protons to the target area, then through two 90° bends onto the target.
- A wobbler magnet that spreads the beam uniformly over the face of the target.

2022 JINST 17 P09042

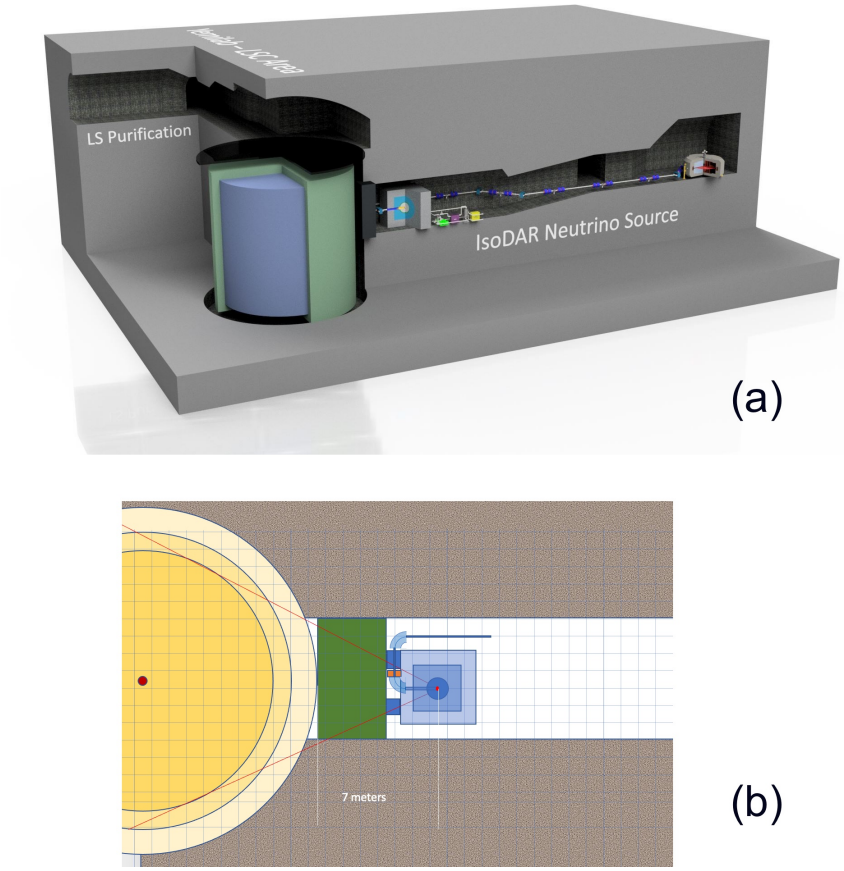

Figure 5. Schematic of the IsoDAR experiment deployed at the Yemilab site; (a) shows the cyclotron at the far right corner and the transport line taking the beam through to the target area. The target assembly is represented by the blue cubes (steel and concrete) in (b), the target itself is the small red dot at the center. The sleeve with the ^{8}Be+^{7}Li where the $\bar{\nu}_e$ flux is produced, surrounds the target. The beam line comes in via two 90° bends so the beam strikes the target pointing away from the detector. This greatly reduces the fast neutron flux directed towards the detector. The target volume of the detector is represented by the blue cylinder in (a) and darker yellow in (b), and the buffer and veto regions are shown in green (lighter yellow in (b)).

- A layered beryllium and heavy-water target that is struck by the proton beam, producing large quantities of neutrons.
- A sleeve containing a mixture of ≥99.99%-enriched ^{7}Li (~ 25%) and beryllium (~ 75%) that is flooded by these neutrons, which are moderated and captured to make the parent ^{8}Li. The subsequent β-decay of the ^{8}Li (839 ms half-life) produces the electron-antineutrinos. Note, the beryllium in the sleeve helps multiply the neutron flux.

The layout of these components in the Yemilab setting is shown in figure 5(a). The cyclotron is placed in the dedicated Cyclotron Room at a bend in the Entrance Ramp to the Target Room. (See also figure 21 for a plan view of the layout.) A large steel and concrete block (shown in green in figure 5(b)) covers the opening to the LSC detector, to shield the detector from gammas and neutrons generated in the Target Room. The two 90° bends in the beam line orient the beam so it strikes the

2022 JINST 17 P09042

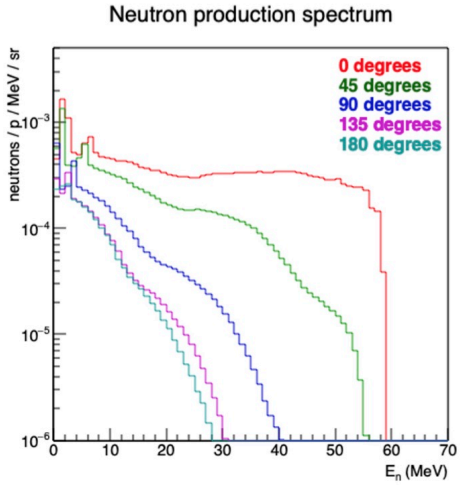

Figure 6. Angular distribution of neutrons emerging from the target. High-energy neutrons in the backwards direction are greatly attenuated, reinforcing the value of the beam entering the target going away from the detector.

target going away from the detector. Figure 6 demonstrates the value of this concept: the flux of high-energy neutrons emitted in the backward direction, towards the detector, is greatly reduced in both energy and intensity. The target of nested shells of beryllium cooled with D_2O stops the beam and produces the neutrons shown in figure 6. These neutrons are moderated as they stream into the sleeve surrounding the target where they are captured by the ^{7}Li. The high fraction ~(75%) of beryllium powder in the sleeve has been optimized to multiply the neutrons, and thus maximize the yield of ^{8}Li [23]. The target and sleeve are surrounded with highly efficient shielding material to minimize neutrons emerging from the shielding structure.

As the purpose of this section is to provide context for the layout underground and the infrastructure requirements, the elements are discussed only briefly. For more substantial information on the components, please see the 2015 Technical Facility CDR on the neutrino source [24]. Updates to that information and substantial detail on the most complex elements of the neutrino source are provided in references [23, 25–28]

2.1 Overview of the accelerator system

IsoDAR will deliver an order-of-magnitude more beam current than existing compact cyclotrons. The standard commercial compact cyclotrons today are limited by space-charge forces, especially at injection energies. One must compress the charged particles into a tight bunch for injection and acceleration into the cyclotron, but the charge in this bunch generates a strong repulsive force (referred to as "space charge") which at high beam currents becomes too large to be overcome by the available focusing forces. A second limit for conventional cyclotrons, all of which accelerate H^-, is the lifetime of the stripping foil used for extracting the beam.

To reach our performance goal, the IsoDAR system must address both of these challenges, and must pay great attention to efficiently bunching, injecting, accelerating and extracting the very high-current beam. In all of this, it is imperative to minimize beam loss. First of all, large beam losses require higher currents from the ion source to ensure adequate beam intensity on target.

2022 JINST 17 P09042

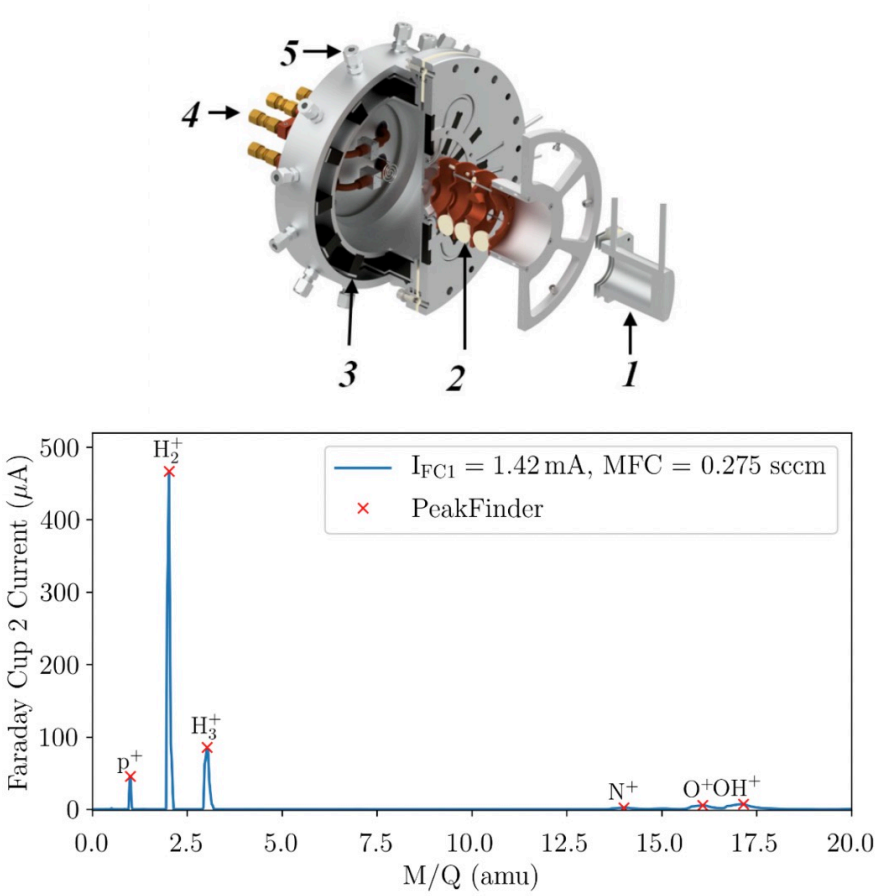

Figure 7. Cutaway of MIST-1, filament-driven H_2^+ source, and recent spectrum. H_2^+ peak dominates over proton and H_3^+, contaminant fraction is low [26].

Secondly, beam losses for high intensity beams can damage the accelerator. At the low energies at the start of acceleration in the central region of the cyclotron, beam loss causes sputtering of material and voltage breakdown; at high energies, beam loss into the walls of the cyclotron produces neutrons that cause activation and severely limit the ability to perform maintenance on the cyclotron because of the high radiation fields.

Three important design breakthroughs will allow us to reach the necessary intensities.

First, we use H_2^+ ions rather than protons, which has benefits at a number of places in the acceleration cycle, not the least being a reduction in space-charge effects. A prototype high-current, filament-driven multi-cusp ion source has been built, shown in figure 7 that also shows the results of first studies of the source [26]. Development and optimization of this source is continuing; at this writing H_2^+ current density and ionic fraction are moving well towards design requirements [29].

Secondly, we employ direct axial injection through an RFQ buncher for the first time in a compact cyclotron, allowing the high efficiency beam capture that is necessary to reach high intensity [27]. This RFQ replaces the conventional "low energy beam transport" (LEBT) that transports the continuous stream of particles from the ion source to the point of cyclotron injection through the so-called "spiral inflector" [30]. For efficient capture, the cyclotron can accept only beam

2022 JINST 17 P09042

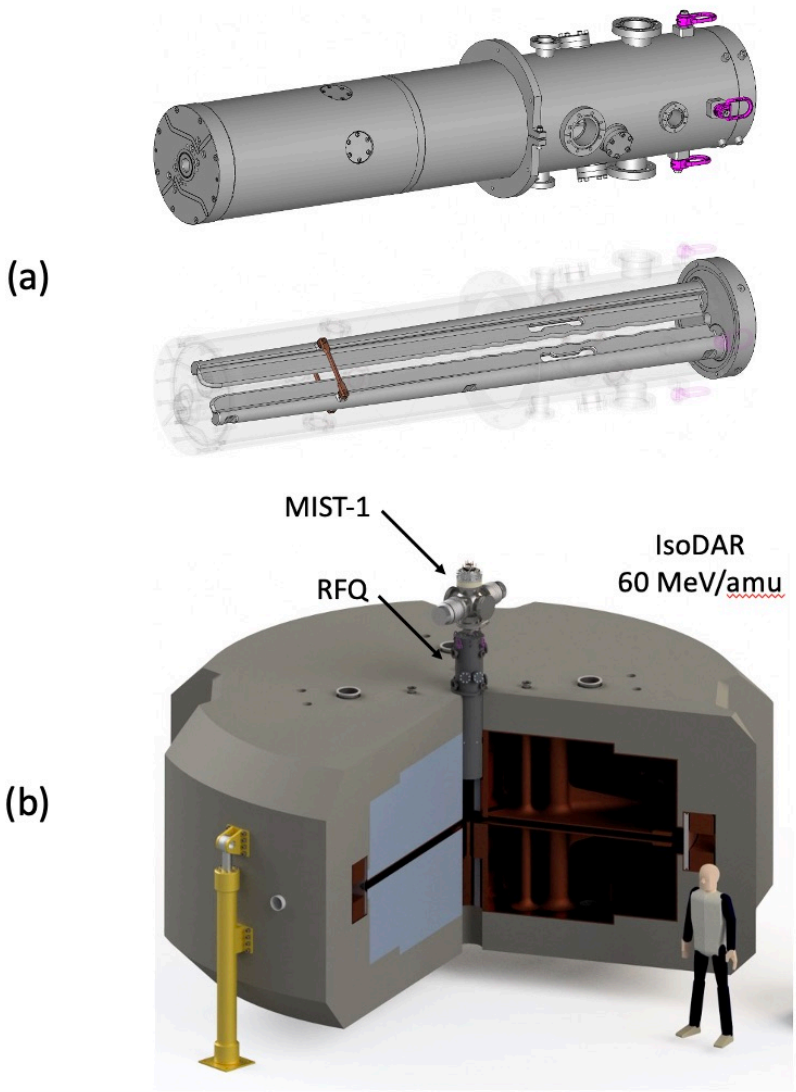

Figure 8. (a) Engineering model of RFQ designed by Bevatech GmBH, Frankfurt. The bottom half of (a) shows two vanes of the split-coaxial structure mounted on one end plate. The other two vanes are mounted on the opposite end plate. This geometry allows for the very low resonant frequency of 32.8 MHz, the frequency driving the cyclotron RF system. The MIST-1 source is mounted on the right side, beam exits from the left side. (b) The RFQ is shown mounted along the central axis of the cyclotron. A bit more than half of the structure is inside the steel of the cyclotron magnet. The exit point is located 20 cm from the first accelerating Dee of the cyclotron. This short flight path preserves most of the bunching provided by the RFQ.

that is within $\sim \pm 10^{\circ}$ of the synchronous phase of the RF accelerating voltage. As beam from the ion source is continuous, capture efficiency is less than 10%. This requires a factor of 10 higher current from the ion source, and leads to large beam losses in the central region of the cyclotron. Because of the high space-charge in low-energy high-current beams, "classical" double-gap bunchers, attempting to compress more particles into the acceptance window, only increase the capture efficiency to about 30%. The 1-meter long RFQ buncher, operating at the same frequency as the cyclotron, is capable of

2022 JINST 17 P09042

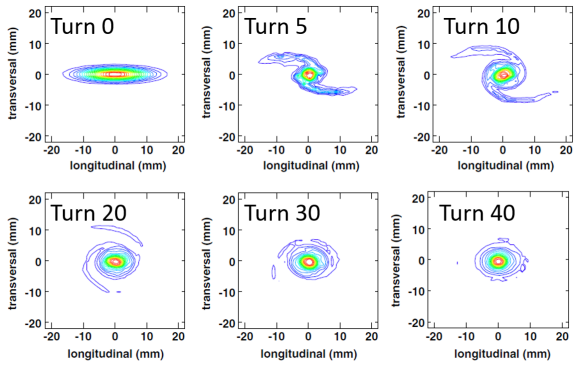

Figure 9. Vortex motion in PSI Injector II; simulations using the OPAL code confirm the experimental observations [31]. In only a few turns the bunch evolves into a spiral, with the majority of the particles wrapped into a tight bunch. Halo particles, amounting to 10–20% of the total, are scraped off with judiciously placed collimators, all before the beam has reached 5 MeV, so causing no activation. From turn 40 onwards there is virtually no change in the bunch shape.

placing over 60% of the continuous beam from the ion source into the phase-acceptance window of the cyclotron and so to increase beam intensity. The RFQ buncher is shown in figure 8. Construction of a prototype RFQ for IsoDAR is now underway [25].

Thirdly, and perhaps the most important breakthrough, was the discovery that for high-current beams in cyclotrons, where space charge is a dominant force, an effect called "vortex motion" can stabilize the beam and reduce growth during acceleration. This surprising finding was first observed at the PSI Injector II cyclotron [32, 33]. As shown in figure 9, as the beam circulates, the combination of space charge effects and external focusing forces induce bunches to curl tightly in phase-space. This prevents the massive losses that some accelerator physicists had predicted would occur on the extraction septum, due to radial overlap of bunches in adjacent turns close to extraction from the cyclotron [31, 34]. The formation of the stable vortices does push a fraction of the bunch into larger "halo" orbits, but these can be removed using carefully-placed collimators, all located in the central region where the beam energy is below the Coulomb barrier so no activation or neutrons are produced.

Instead of extracting the beam with a stripping foil, we revert to the early technique of an extraction channel employing a thin electrostatic septum for guiding the beam out of the cyclotron. For this to work, one must have good turn-to-turn separation at the last orbits, and must keep the size of the bunch small in order to have few particles at the radius where the septum is located. Introducing a structure resonance helps increase turn separation at the extraction point [35], while the above-mentioned vortex effect controls the bunch size. The result, shown in figure 10 shows that the loss on the septum will be less than 100 watts which, considering the total beam power is 600 kilowatts, is a remarkable accomplishment. This level of beam loss is well below the "rule-of-thumb" from PSI, of maintaining beam losses below 200 watts to enable hands-on maintenance of accelerator components.

Placing a narrow stripping foil just upstream of the septum intercepts ions that would strike the septum. These H_2^+ ions are converted to protons which are then bent inwards by the cyclotron magnetic field, and miss the septum. They orbit tightly in the strong "hill" section of the magnetic field, and emerge in the weaker "valley" on a trajectory that takes them safely out of the cyclotron. The details of this extraction scheme are shown in figure 10.

2022 JINST 17 P09042

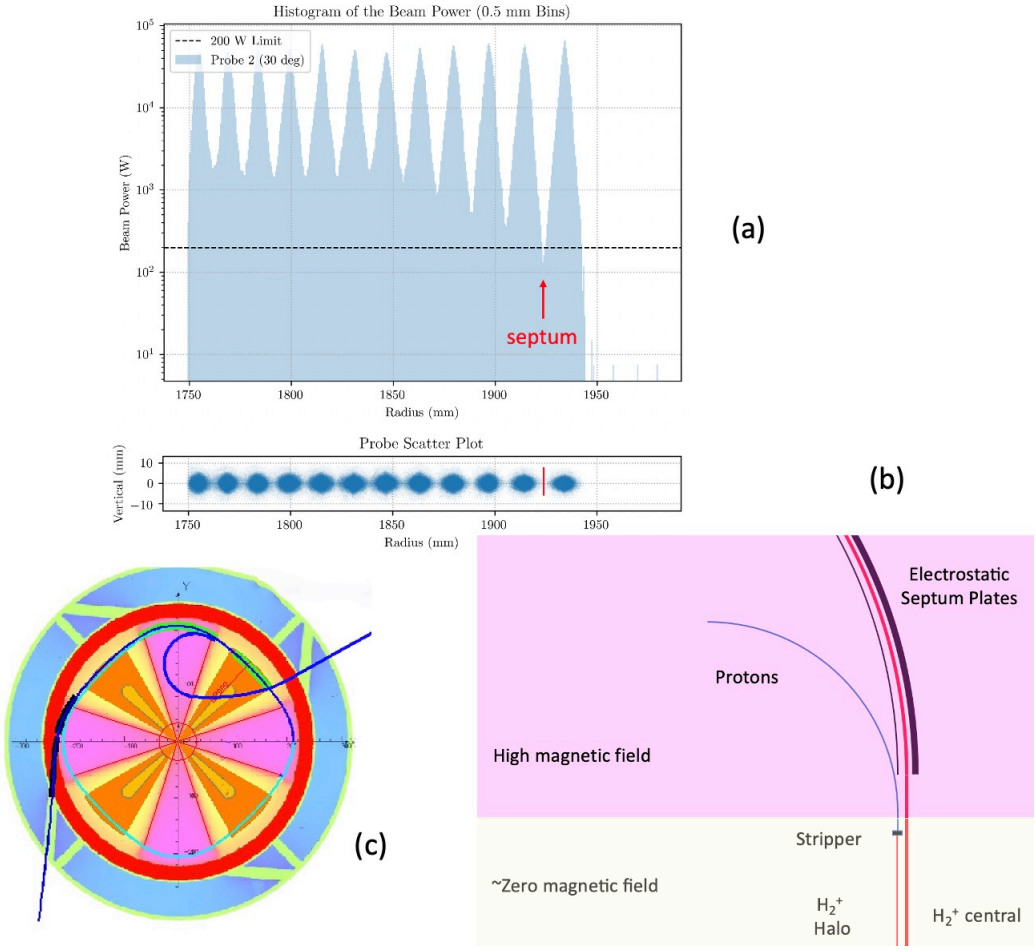

Figure 10. (a) Simulations of outer orbits in the cyclotron showing clean turn separation, particularly on the last turn. Note the logarithmic scale. (b) Schematic of the electrostatic extraction channel (black) and the H_2^+ beam being extracted (red). Residual beam between turns, referred to as "halo" that would strike the inner septum plate is intercepted by the thin stripper. These ions are converted to protons that are more sharply bent in the high "hill" magnetic field of the cyclotron, missing the septum plate. (c) Plan schematic of cyclotron showing the four high-field "hills" (pink), the four low-field "valleys" (yellow), the orange RF accelerating Dees, the red coil surrounding the entire pole section, and the blue yoke return steel for the magnet. The H_2^+ extraction channel is shown with two electrostatic deflectors followed by two magnetic channels. The orbits of the stripped protons are also shown as the blue spiral exiting to the upper right.

2.2 Beam Transport (MEBT) System

Figures 5 and 24 show the transport line connecting the cyclotron to the target referred to as the MEBT (Medium Energy Beam Transport).

The H_2^+ ions extracted from the cyclotron are passed through a thin carbon stripping foil that removes the electron, leaving two bare protons. The stripping system and an analyzing magnet are placed close to the extraction point. The analyzing magnet steers protons into the transport line, and serves to monitor the integrity of the stripping foil. A detector placed at the orbit of unstripped H_2^+ ions picks up impending failure of the foil. A chain mechanism quickly brings a new foil into position.

2022 JINST 17 P09042

Beyond the stripping stage, the proton beam is transported down the ramp to the target area. Standard transport elements are used: quadrupole magnets for focusing and dipoles for bending the protons. Beam position and profile are monitored by standard beam diagnostic devices designed for high-current beams.

Collimation stages at necessary points along the line remove halo from the beam, these "controlled" beam loss points are enclosed in localized shielding to attenuate the neutrons produced from stopped particles.

The remaining "uncontrolled" loss is from scattering of protons in the residual gas in the beam line, which occurs along the length of the line. The scattering cross section for protons is substantially less than for H_2^+ ions, justifying the stripping of these ions as soon as possible after the extraction point. This loss is mitigated by specifying the highest practical vacuum in the beam line.

As described earlier, the two 90° bends bring the beam onto the target going away from the LSC, decreasing the flux of fast neutrons pointing towards the LSC.

The beam is spread out with a wobbling magnet to paint the beam over the face of the target, making the distribution of power over the target as even as possible.

2.3 Target system

The target assembly, referred to as the "torpedo" (see figure 11), is designed for easy removal and replacement from the back of the target shielding block. Figure 12 shows the shielding structure surrounding the target and sleeve, with a 20 cm (inner diameter) vacuum pipe running the full length. The inlet side brings the beam onto the target face. The back side allows the torpedo to be slid out. As mentioned earlier, the orientation of the target assembly in the hall faces away from the detector (See figure 5(b)), and so provides ample room for removal of the long torpedo assembly. This will probably be done remotely, using a robot, because of high radiation levels. The spent targets will be stored in bore holes drilled into the walls of the target hall, as described in 3.1.3, and shown in figure 24.

The head of the torpedo, the actual target struck by the protons, consists of three nested beryllium hemispheres each having a thickness of 3 mm with a gap of 7 mm of heavy water between them, shown in figure 13. Heavy water is used as the cooling fluid, as the absorption cross section for neutrons is

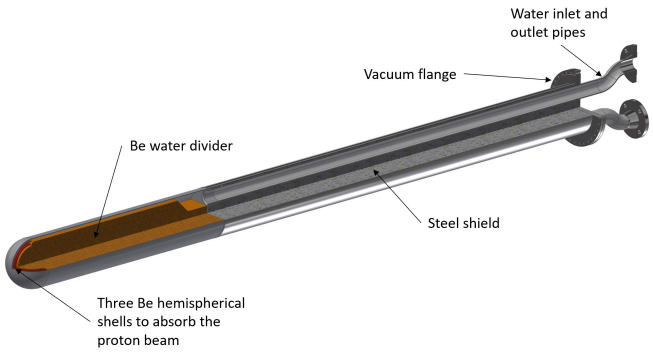

Figure 11. Referred to as the "Torpedo," the target assembly consists of nested beryllium hemispheres separated by cooling water (D_2O) channels. The entire assembly can be easily detached from the cooling lines and removed into a shielded storage area.

2022 JINST 17 P09042

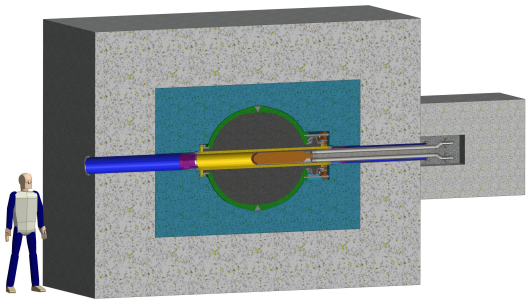

Figure 12. Section through the target system and the surrounding shielding. The target torpedo is surrounded by a Li/Be sleeve pressure vessel. The shielding consists of inner layers of steel (shown in blue) and outer layers of boron rich concrete (shown in grey).

lower, and there are added neutrons from the breakup of the deuteron. GEANT4 calculations indicate an almost 40% improvement in the ^{8}Li yield for D_2O over H_2O. Using heavy water does introduce tritium issues, however, the completely-sealed design of the primary cooling loop assures that tritium will not be released into the environment. Mitigation of tritium will be considered as part of a future decommissioning plan, where recovery and purification of the heavy water will be addressed.

Water is circulated onto the target using a central divider plate made of beryllium, to separate the water flow. Water flows smoothly through the gaps between the beryllium hemispheres, Computational analyses of heat flow, temperature profiles and thermal stresses at the boundaries indicate acceptable performance of this target design, and show the target can handle the 600 kW of beam power. The target geometry is still being optimized, specifically to address the known issue of blistering of beryllium at the stopping point of the proton beam under intense bombardment due to the low solubility of hydrogen in beryllium [36]. The beam was modeled with a uniform energy distribution across the face of the torpedo filling an 18 cm diameter circular area. The target flows 500 gallons of water per minute, (0.031 m^3/sec), with an inlet temperature of 60° F (15.56° C). The pressure drop

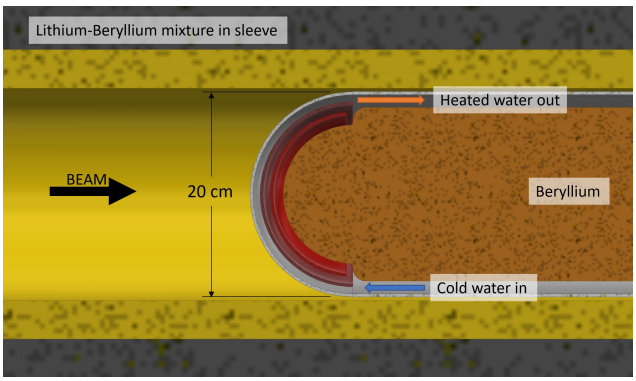

Figure 13. Inside of the target vessel. The beam is spread out over the face of the target by upstream wobbler magnets running at least at 50 Hz. Cooling is provided by circulating heavy water that also serves to generate more neutrons. Protons, with a range of about 2 cm, are stopped at various depths in this structure (depending on radial position). Neutrons stream into the sleeve surrounding the target, consisting of a mixture of highly enriched (> 99.99%) ^{7}Li and beryllium. ^{8}Li is produced by neutron capture.

2022 JINST 17 P09042

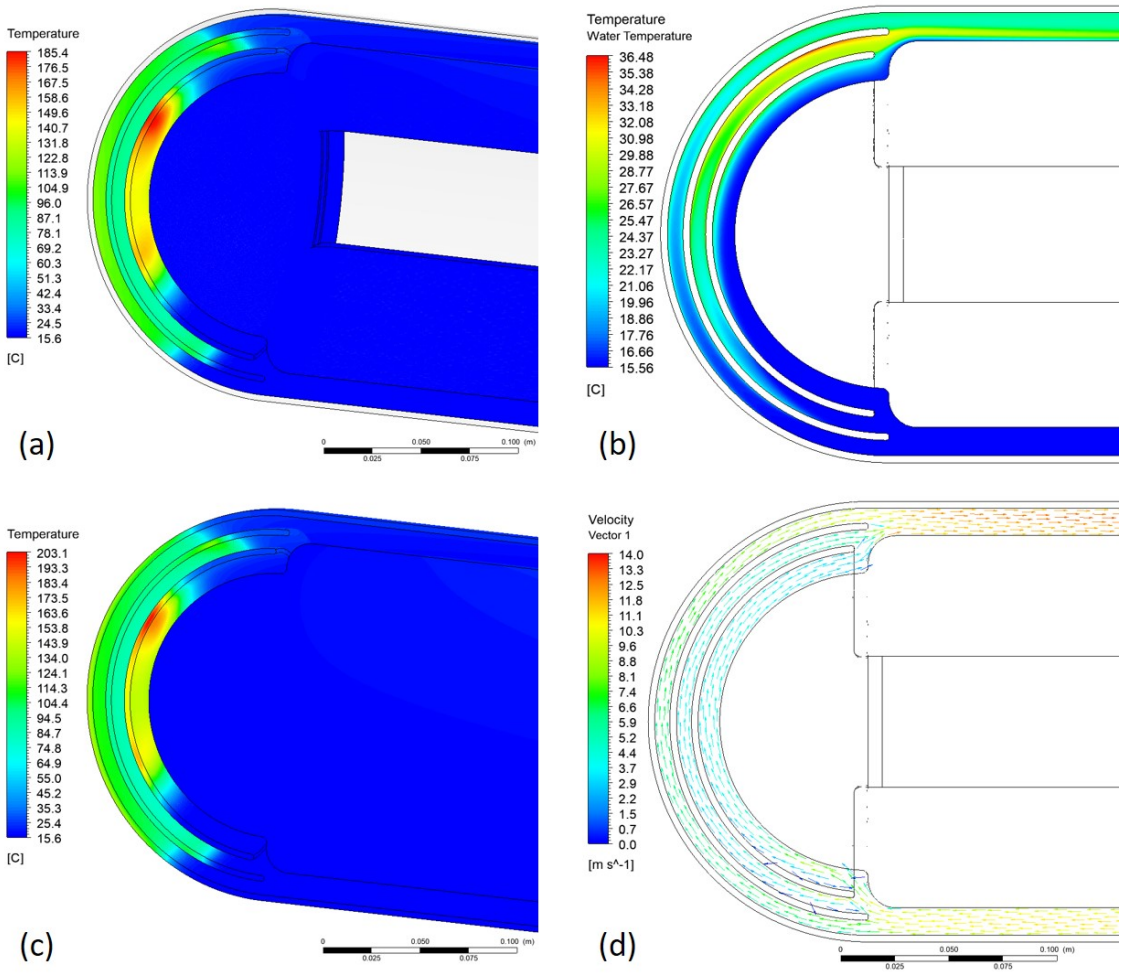

Figure 14. (a) Temperature at the interface between beryllium and water. (b) Bulk water temperature away from the interface with the beryllium. (c) Beryllium temperature at the 500 GPM water flow rate. (d) Velocity vectors at the vertical mid-plane of the torpedo.

across the target at this flow rate is 30.4 psid (209.6 kPa). The Computational Fluid Dynamics (CFD) analysis was single phase only. Figure 14 (a) shows the temperature of the beryllium-water interface.

Figure 14(b) shows the bulk water temperature away from the Be/water interface. Water temperatures are quite low away from the interface. A future study will determine how far away the design is from the critical heat flux. The interface temperature is higher than the boiling point of water at 1 atm, but the boiling temperature may be increased by increasing the pressure of the water. 100 psi (689.4 kPa) static pressure was applied in this model. Two-phase analysis of the water cooling will happen once the actual energy distribution from the beam line is known.

Figure 14(d) shows the velocity distribution in the water and shows good flow development between the beryllium hemispheres. The single-phase analysis was primarily to look at the thermal stress in the beryllium as this was a problem in earlier designs. The single-phase temperature distribution in the beryllium is more conservative because introducing boiling will reduce the beryllium temperature. Thermal stresses were analyzed per the methods of the ASME Boiler and

2022 JINST 17 P09042

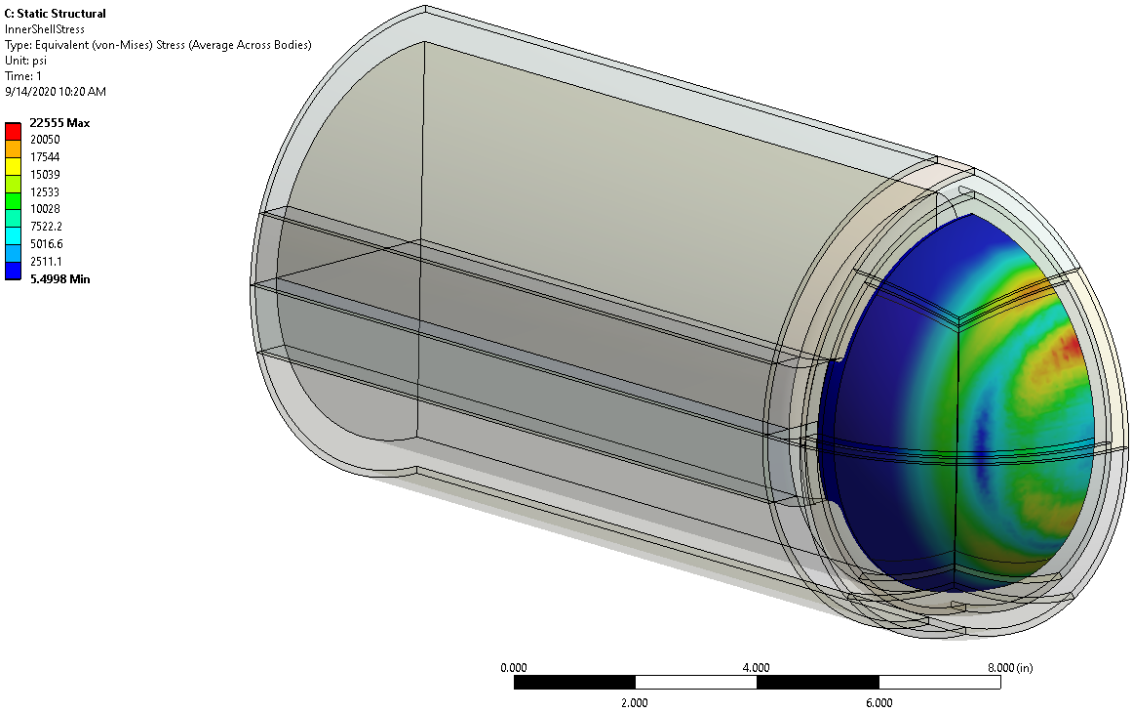

Figure 15. Thermal stress (Von Mises stress) on the innermost beryllium hemisphere.

Pressure Vessel Code Section 8, division 2. Figure 14 (c) shows the temperature distribution in the beryllium. Figure 15 shows the maximum thermal stress in the beryllium, which happens on the innermost hemisphere. The maximum stress there is 22.6 ksi (155.8 MPa) and the allowable stress is 36 ksi (248.2 MPa). Stresses on the outer hemispheres are lower. This analysis showed that the target has sufficient cooling characteristics to allow the long-term survival of the beryllium to thermal stress.

The target torpedo is surrounded by the sleeve containing 25% ^{7}Li and 75% ^{9}Be. It is a roughly spherical pressure vessel with an outer radius of 84 cm, and an inner radius of 74.4 cm. The sleeve is filled by pouring liquid lithium into the sleeve pre-loaded with beryllium powder. The sleeve vessel is rated at 2500 psi, owing to the need to load the liquid lithium under pressure because of the significant decrease in volume between liquid and solid phases of the lithium. Not doing so would introduce unacceptable voids in the sleeve material.

The sleeve was also analyzed by the methods of the ASME Boiler and Pressure Vessel Code, section 8, Division 2. The materials in the model are shown in figure 16. The model showed that a plain carbon steel sleeve does not satisfy the ASME allowable stress. The sleeve material was changed to a structural steel, DIN K13049. Bolts are Inconel 718 and threaded rods in the model are B22 steel. The analysis showed that the vessel satisfied the ASME stress allowable, but a peculiarity of the Code is that it is only concerned about whether a vessel is safe to internal pressure, not whether or not it leaks. It is imperative that molten lithium not leak out during the fill process, so much time was spent looking at the deformation of the o-ring grooves that seal the liquid lithium.

The molten lithium is sealed in this design by custom Helicoflex metal seals. The seals crush by 0.021″ (0.53 mm) minimum. Figures 17 and 18 show the seal configuration. Figure 19 shows how the deformation of the o-ring groove changes through the application of the load cases of the analysis.

2022 JINST 17 P09042

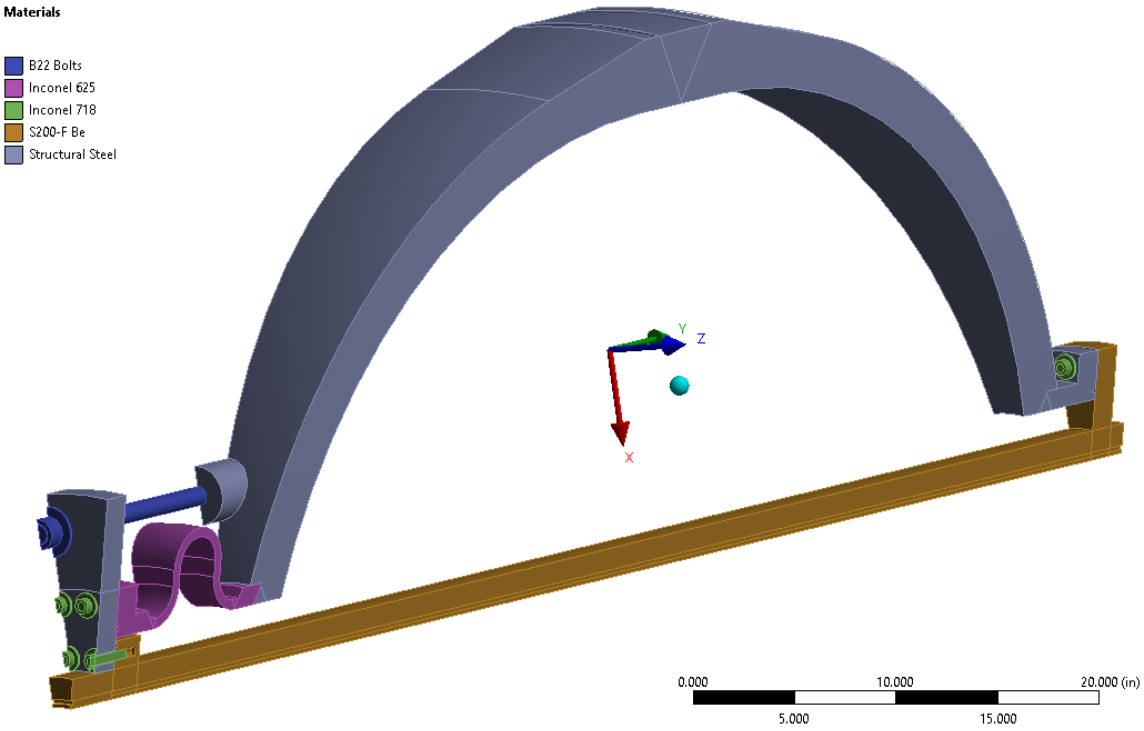

Figure 16. Model (15° symmetric wedge) of the sleeve as a pressure vessel showing the materials at different locations.

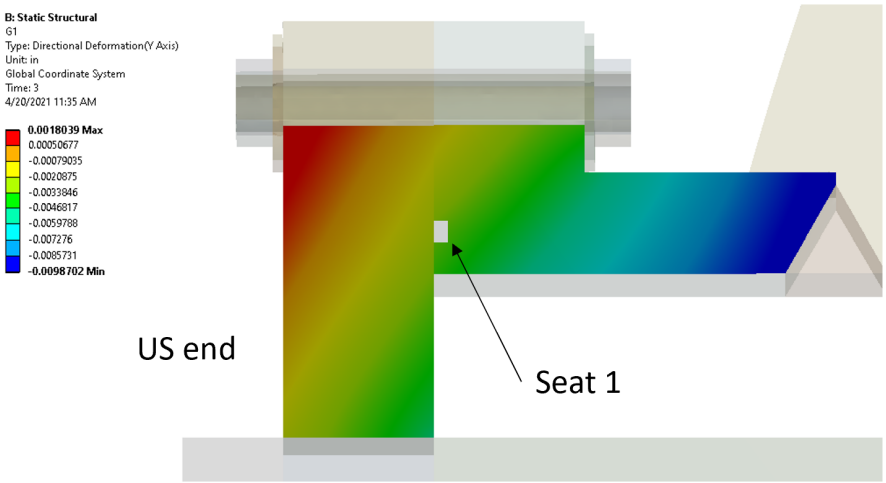

Figure 17. Deformation around the upstream (US) o-ring groove.

Gasket seat 3 is of concern because as pressure is increased in the model, the deformation always increases. Gasket seats 1 and 2 show a decrease in deformation as the pressure is applied. In any case, the maximum deformation is about 0.001″ (0.025 mm) at 2,500 psi (17.24 MPa), or 4.8% of the seal crush. It is impossible to determine with certainty from these analyses whether the seals will leak, so prototyping the seals will happen in parallel with the development of the lithium injection machine.

2022 JINST 17 P09042

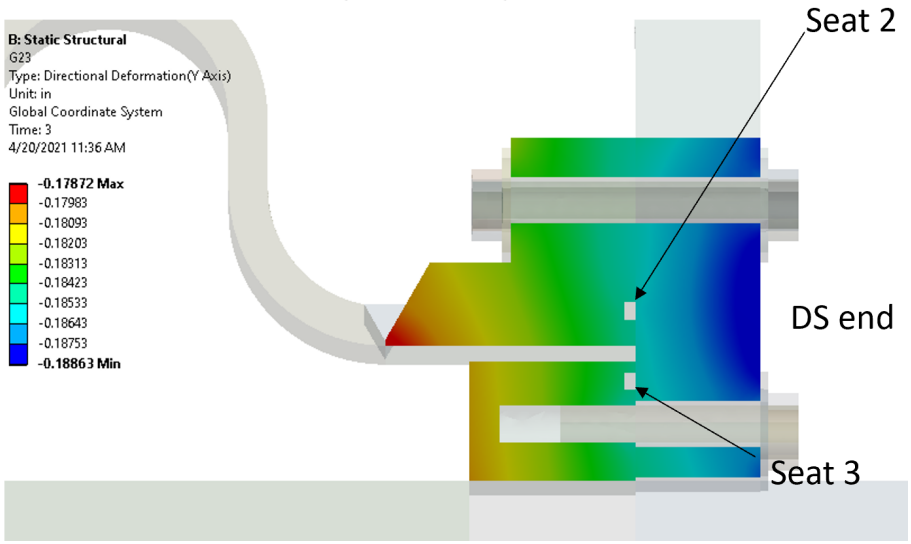

Figure 18. Seal configuration at the downstream (DS) end showing deflections.

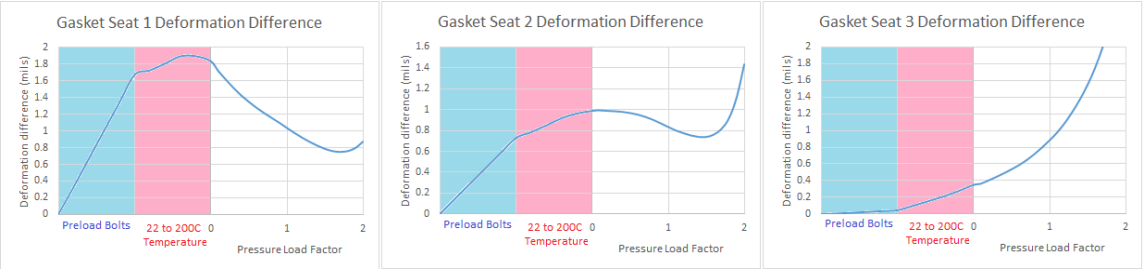

Figure 19. Gasket seat deformation differences (in thousandths of an inch,) as the loads are applied to the model.

Beyond the sleeve is the shielding enclosure (cf. figure 12), consisting of steel cylinders and plates, with a nominal thickness of 30 cm, and boron rich concrete of minimum thickness of 90 cm. Specifications and design details for this shield are addressed further in section 3.2.

3 Installation at Yemilab

Yemilab is an ideal location for the installation of IsoDAR for many reasons: access to the underground site is possible with trucks to bring components directly from the surface; ample space is available for an optimal layout for the experiment, allowing for separation of the cyclotron from the target by many meters — such a layout allows for convenient installation and maintenance of equipment; excavation of the cavern space fits in perfectly with the Yemilab construction timetable, in fact this construction is underway at present. In addition, the limestone rock environment is very dry and has a very low sodium content, reducing rock activation and eliminating need for ground-water management. Finally, the LSC detector will have a sensitive liquid scintillator mass of 2.26 kilotons which allows for excellent physics reach. All these points will be (or have been in the case of the physics potential) elaborated further in this document.

2022 JINST 17 P09042

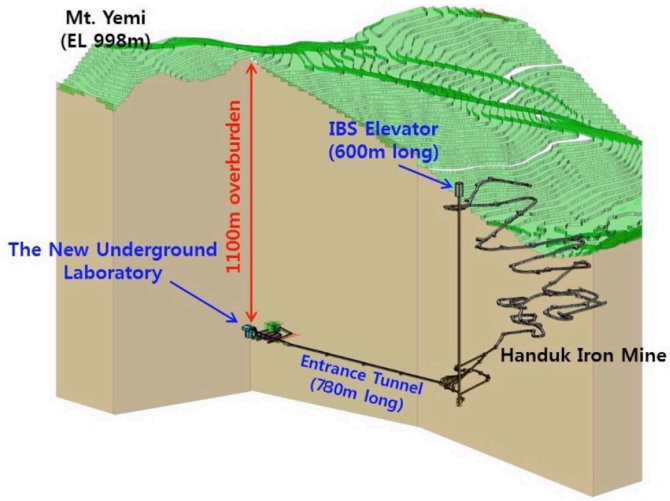

Figure 20. The location of Yemilab underneath Mount Yemi, adjacent to the Handuk Iron Ore Mine, about 200 km Southeast of Seoul. Access to the Laboratory level is via the 6.6 km mine ramp. Personnel access is also available using the elevator shaft.

We describe the cavern spaces in section 3.1 and requirements for shielding in section 3.2. Installation of IsoDAR is considered in section 3.3 and requirements for electric power and other utilities in section 3.4.

3.1 Yemilab description

The Yemilab complex is shown in 3-D in figure 20. The Laboratory is located close to the Handuk Iron Mine, which has a truck-accessible ramp winding downwards for 6.6 km, and slope ranging between 12% and 15%. From the base of this ramp (and also the terminus of a vertical personnel conveyance), the 780-meter long (12% slope) Entrance Tunnel leads to the Laboratory. The Laboratory is a complex of about 9,000 m^2 with 26 laboratories and support rooms arranged in a ladder pattern. The Entrance Tunnel levels off into the Primary Yemilab Drift, the backbone for the system of crossing laboratory spaces. The cylindrical LSC Hall (20 meter diameter × 20 meter high) is close to the start of the backbone drift. This cylindrical hall is capped by a domed 22 × 22 meter cavern providing access to the top of the detector and housing electronics and infrastructure. The drifts built for excavation and rock removal from the LSC Hall will be the location for the IsoDAR equipment.

All Drifts and Ramps in the mine and Yemilab areas are nominally 5 × 5 meters, though some areas have more restricted cross sections because of ceiling-mounted ventilation trunks or other infrastructure needs. Designated Rooms are usually larger.

3.1.1 Overview of IsoDAR cavern spaces

The primary IsoDAR cavern spaces, shown in figure 21, consist of

- The Entrance Ramp — 5 m (wide) × 5 m (high) × 45 m (long);
- The Cyclotron Room — 17 m (deep) × 12 m (wide) × 10 m (high);

2022 JINST 17 P09042

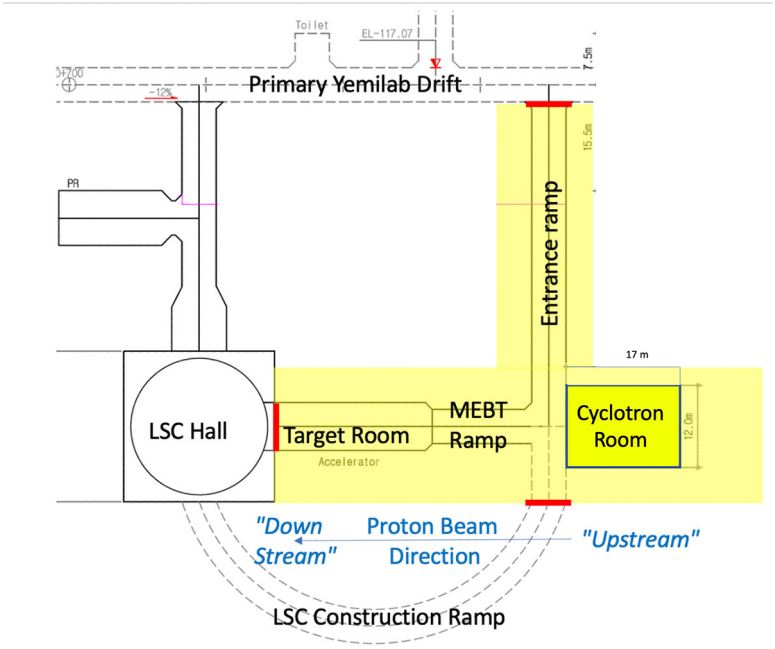

Figure 21. Layout of IsoDAR caverns at Yemilab. These areas include the Entrance ramp, as the principal access to the IsoDAR experiment. This ramp drops about 6 meters to the Cyclotron Room, then another 2 meters via the MEBT Ramp to the Target Room. The Target Room intercepts the LSC Hall at about the vertical half-way point. All these ramps and rooms, except for the Cyclotron Room, are used for rock removal from the LSC Hall.

- The MEBT Ramp — 5 m (wide) × 5 m (high) × 15.5 m (long); and
- The Target Room — 7 m (wide) × 7 m (high) × 22 m (long).

The cavern cross sections are all arched, or horse-shoe shaped, for rock stability: so the height in the Ramps and Target Room is the maximum height of a semicircular arch of radius 2.5 m (Ramps) and 3.5 m (Target Room). The dome of the Cyclotron Room, as seen in figure 22 is less arched, but has longer rock bolts. The Ramps have 12% slopes, while the floors of the Rooms are flat. The floor of the Cyclotron Room is about 6 meters below the level of the Primary Yemilab Drift, the Target Room is another 2 meters lower. The Target Room connects to the LSC Hall at the vertical mid-point of the LSC detector. The semicircular Construction Ramp allows removal of rock from the bottom level of the LSC Hall.

All these spaces are required for the excavation of the LSC Hall, except for the Cyclotron Room, which is being excavated at the same time (figure 22 shows the now-completed Cyclotron Room). The construction of the LSC Hall and all the IsoDAR caverns will be finished by the end of February, 2022. This is the last phase of major construction at the Yemilab site. Formal commissioning of the Laboratory and installation of the first experiments will follow.

It should be noted that large mining trucks are being used for removing rock from the construction sites, and that these trucks can navigate all the turns and sharp corners in the ramp and tunnel system. These same trucks will be bringing cyclotron and other components into the IsoDAR area for assembly.

2022 JINST 17 P09042

Figure 22. Completed Cyclotron Room excavation.

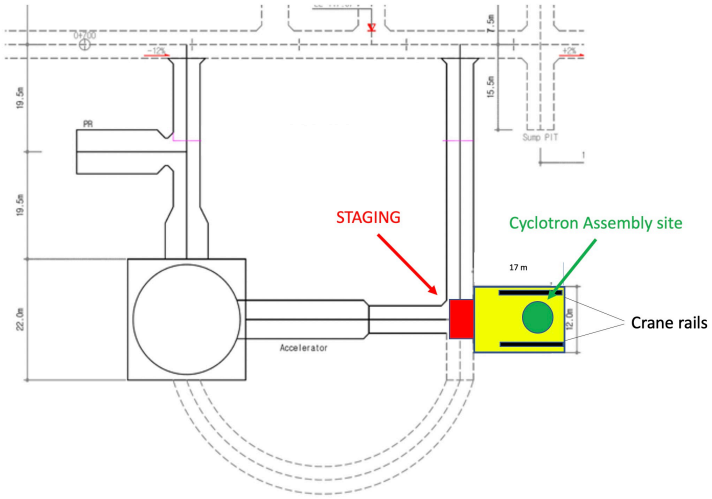

Figure 23. Plan view of the Cyclotron Room. Note the staging area at the base of the Entrance Ramp, and the approximate location of the cyclotron. Also notice the rails for a bridge crane, highly valuable for the assembly of the cyclotron.

3.1.2 The Cyclotron Room layout

The size of the Cyclotron Room must be adequate both for operations needs and for assembly and installation of all the technical components.

The cyclotron is quite compact, at 6 meters' diameter. There are some critical elements, such as the final RF amplifiers that need to be relatively close by as the high-power lines between these and the cyclotron Dees must be as short as possible. Vacuum pumping equipment must also be nearby. Other elements can be located elsewhere, possibly even outside the main IsoDAR areas for easy access and maintenance. Cable trays will provide the pathway for connection of these units and the cyclotron.

2022 JINST 17 P09042

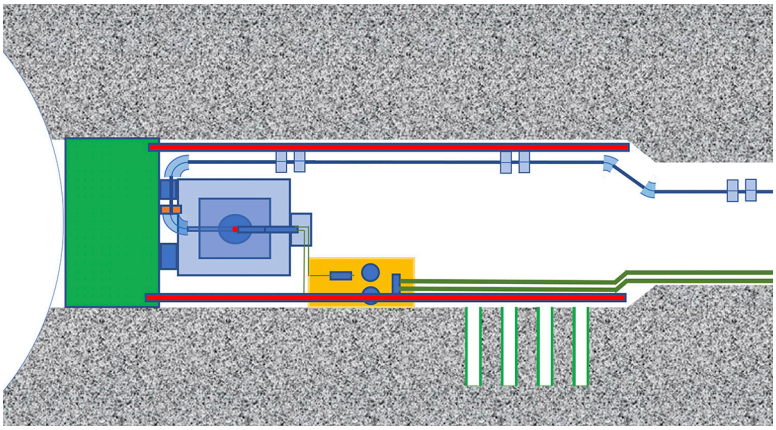

Figure 24. Plan view for the conceptual layout of the Target Room. The MEBT beamline is seen along the top edge of the plan. Beam enters from the right and is directed by two 90° bends to the target at the center of the large shielding block at left, in blue, next to the shielding wall (indicated in green) designed to prevent neutrons from reaching the LSC. The orange rectangle indicates a utilities-skid. Red lines indicate crane rails. Bore-holes for spent targets are shown at lower right. See text for further explanation.

But in the end, the size of the Cyclotron Room is set by the needs for assembly of the cyclotron. Figure 23 shows a conceptual configuration for the Cyclotron Room, including a staging area at the base of the Entrance Ramp where components can be taken off of the truck (using a fork lift, for example) and moved into a laydown area adjacent to the cyclotron assembly point. The cavern size allows for a minimum of 3 meter clearance all around the cyclotron, and also for a bridge crane to facilitate assembly. The specification for this crane will be done in conjunction with the (as yet to be selected) cyclotron builder, and will be related to the maximum weight of component pieces of the cyclotron steel.

One additional feature of the Cyclotron Room is that the cavern floor must provide a foundation capable of supporting the 450 ton weight of the cyclotron. Thick (~ 10–20 cm), large (~ 1–2 m^2) steel plates must be set in the floor under the cyclotron support points to distribute the load.

3.1.3 The Target Room layout

A conceptual layout of the Target Room is shown in figure 24. This figure shows the beam line bringing the 60 MeV protons to the target in the center of the large shielding block of iron and boron-loaded concrete.

The geometry pictured provides a solid angle of ~ 0.2π steradians for neutrinos produced in the sleeve, or roughly a 5% efficiency for the $\bar{\nu}_e$'s produced to reach the fiducial volume of the detector. Maximizing the solid angle, i.e. the experimental efficiency, requires placing the target as close as possible to the detector. However, adequate shielding must be provided to ensure neutrons do not reach the fiducial volume. The geometry for the experiment is a careful balance between these two factors.

Cooling for the target is provided by the pumps, filters and heat exchangers shown on the yellow skid in figure 24. As the (heavy) water circulating here comes directly from the very high radiation environment of the target area, it must be treated as RAW (RadioActive Water) with full containment. If major maintenance of these components is required, the entire skid can be placed in a shielded container and removed to the surface to a suitable hot cell area where repairs

2022 JINST 17 P09042

or component replacement can be safely conducted. Heat exchangers on the right-most side of the skid transfer heat to the secondary water system pipes, shown in green. These heat exchangers also provide environmental isolation of the two water systems. The secondary water system, and eventual conduction of the heat to the surface, will be discussed below in the section on utilities.

An important element of the Target Cavern is provision for target changes. Over the 5 years of IsoDAR operation, targets will need to be replaced. We are drawing on experience at high-power-beam installations (for example, Fermilab, SNS, JPARC, ISIS after) in developing target-changing procedures. Space within the hall is adequate for this operation. Spent targets must remain within the target space for several years to cool before transport to the surface. For storage, we are proposing that a series of $\sim$ 25 cm diameter bore holes be drilled in the wall of the cavern. These are shown schematically in figure 24 as the four perforations in the lower wall, right. A detailed study will establish the desired number of such storage bore holes. The bore holes will be made deep enough to accommodate a steel plug of $\sim$ 0.5 meter to block the opening.

A medium-capacity bridge-crane system will ease construction and can be used during initial assembly, and for target-changes. The capacity of this will be in the 10–15 ton range. The crane rails are shown in red in figure 24.

3.2 Shielding considerations

As the neutrino flux delivered to the detector is directly related to the number of neutrons produced in the target and sleeve, management of these neutrons must be given close attention. This relates to shielding, as well as environmental isolation of the IsoDAR area from the main Yemilab complex. The latter is greatly facilitated by the single point of connection between the IsoDAR caverns and the body of the laboratory. The top of the entrance ramp will be sealed by a properly-designed door that is closed except to allow entry of personnel, probably through an airlock that allows a slight negative pressure to be maintained on the IsoDAR side.[1] An extensive labyrinth will also be placed behind this door to prevent neutron migration.

Radiation levels when the cyclotron is delivering beam will be high, no personnel will be allowed inside the IsoDAR space under these conditions. When the beam is turned off, residual radiation levels will be related to the amount of activation in the material and walls of the caverns caused by neutrons not stopped in the (neutron) shielding, and to the (gamma) shielding between these activated materials and the rest of the caverns.

Shielding requirements can be divided into short-term (hours or days after beam shutoff), or long-term (years after last beam). The former relates to gamma radiation fields experienced by personnel entering for maintenance activities, the latter to the final decommissioning of the experiment, and ensuring that, after decommissioning, radiation levels in the caverns are safely below Korean regulatory limits. As gamma radiation comes from decay of isotopes produced by neutron reactions, the critical consideration is the half-lives of these isotopes. Figure 25 traces a typical activation curve, showing the buildup of activity during the experiment for material exposed to neutrons, and after the beam is shut off, the decay of this activity level.

[1] A single egress point requires the installation of a Refuge Chamber in the Target Room for underground safety. The number of persons allowed beyond the barrier door is limited to the capacity of this Refuge Chamber.

2022 JINST 17 P09042

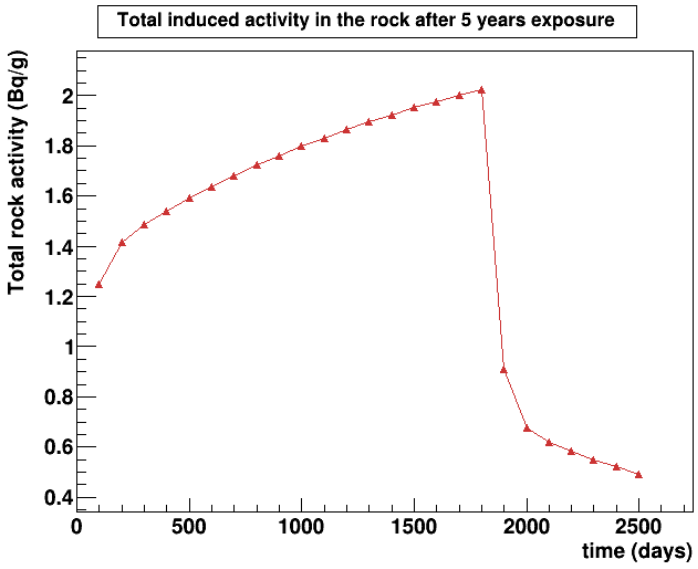

Figure 25. The curve shows the buildup of activity in the surrounding rocks for the 5-year beam-on-target period. Once beam is shut off after 1825 days, rapid decay of the many short-lived isotopes occurs, leaving only long-lived activities described in 3.2.1. The "end of the experiment" is declared at approximately day 2500, by which time the activity level has dropped very significantly. The vertical scale should be viewed as arbitrary, it depends strongly on the composition of the rock.

3.2.1 Long term activation considerations

When evaluating residual radioactivity in the caverns, only the rock of the walls needs to be considered. Components that are brought in that may be activated will be removed after the experiment for safe disposal elsewhere, only the rock will remain.

The tail in the curve of figure 25 in the case of Yemilab is due to just a few isotopes with half-lives longer than a few years, primarily ^{60}Co (5.3 years), and ^{152,154}Eu (13.5, 8.6 years), produced by thermal neutron capture; and ^{22}Na (2.6 years) when high-energy neutrons are present (the (n,2n) reaction has an 11 MeV threshold). Assays of Yemilab rock (basically pure limestone) from the vicinity of the LSC Hall have yielded very low concentrations of Co (< 10 ppm), and Eu (< 1 ppm), but far more important is that the sodium concentration is exceedingly low (0.02%).

An extensive GEANT4 study has been performed (described in detail in Chapter 5 of the CDR), resulting in the design of the shielding structure around the target and sleeve (layers of steel and boron-loaded concrete), and an evaluation of residual rock activity at different depths from the rock face. For the case described above, 2 years after the final shutoff of beam, the highest concentration of activity (seen directly above the center of the target, in the first 10 cm of rock depth) was less than 0.05 Bq/g. The Korean regulatory requirement allows a maximum of 10 Bq/g. The exceedingly low value is a direct result of the favorable concentration of sodium in the rock.

3.2.2 Short term activation considerations

When access is required for maintenance or repair, background radiation results from decay of isotopes with half-lives in the hour-range. In accelerator environments, two isotopes stand out

2022 JINST 17 P09042

as major contributors: ^{24}Na (15.0 hour) and ^{64}Cu (12.7 hour), both are produced by capture of slow neutrons, and emit gammas in the 0.5 to 5 MeV range. Again sodium is the most damaging environmental component and, as indicated above, Yemilab native rock carries very low sodium content. It is important to ensure that material brought into the caverns, primarily for rock surface finishing (shotcrete) or as concrete shielding blocks, is also low in sodium. Copper is present in all the cables and magnet windings, but these are localized sources, and if activated can be shielded with portable high-Z panels that can be brought in for this purpose. When access is required, a radiation technician will survey the caverns, identify areas requiring localized shielding, and establish when, and for how long, personnel may work in these areas.

3.2.3 Neutron background in the LSC

Background events caused by fast neutrons (above 3 MeV) affect the sensitivity of the LSC. Natural backgrounds, from spallation caused by high energy muons penetrating from the surface, natural U/Th/K concentrations in the environment of the detector, and impurities in the detector material itself, are well understood and characterizable. It is important that the fast neutron flux penetrating from the Target Room that could reach the fiducial volume is kept well below these background levels. The thick steel and concrete wall, shown in figure 24 as the green structure blocking the area between the Target Room and the LSC Hall, must accomplish this. The CDR document describes the state of design for this wall, it is at least 4 meters thick, primarily of steel but with a component of concrete to absorb slow neutrons that are not easily absorbed by the iron itself.

3.2.4 Shielding in other areas

Though the highest concentration of neutrons occurs at the target, beam loss at any location inside the cyclotron and in the transport line to the target will also produce neutrons. Though at much lower concentrations, these loss points must be understood and addressed for shielding design.

The cyclotron is basically a large block of steel, providing self-shielding for neutrons. Maintenance inside the cyclotron that requires splitting the cyclotron apart will be supervised by a radiation technician who monitors the gamma levels and ensures personnel safety through proper localized shielding. Some areas of the cyclotron steel are thinner, and may require special localized shielding around the cyclotron to prevent fast neutrons from reaching the walls of the cavern. Further studies will be performed when the cyclotron design has been completed.

It is not possible to prevent all losses in the MEBT (Medium Energy Beam Transport) line, but they can be minimized, and the effects properly managed. These losses will come from scattering by residual gas in the vacuum pipes, and from growth of beam halo in the transport line. The former is managed by transporting protons instead of the H_2^+ ions extracted from the cyclotron (eliminating dissociation of the H_2^+ ion), and specifying the highest practical vacuum in the beam line ($< 10^{-5}$ Pa). The latter is managed by introduction of collimation stations that scrape the halo particles off of the beam. These areas will receive appropriate shielding to contain neutrons produced. Such areas are referred to as “controlled” loss points; inevitable beam loss is localized to areas that can be properly shielded. The point where the H_2^+ ions are stripped, close to the extraction point, is one such controlled loss point.

2022 JINST 17 P09042

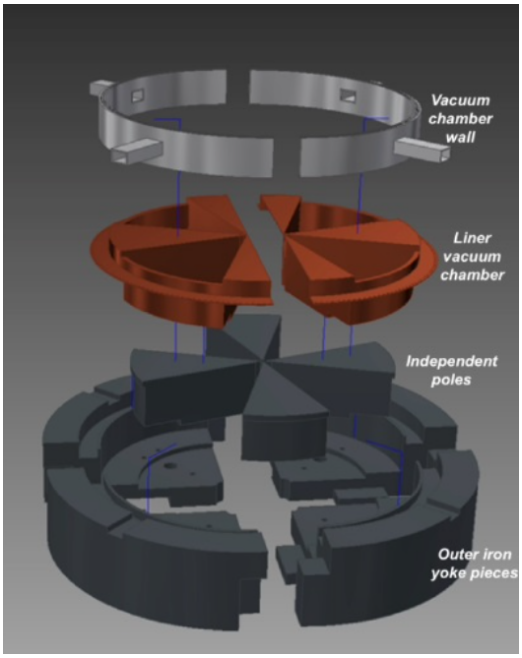

Figure 26. Bottom half of cyclotron, split into parts. The top half duplicates the liner (red) and magnet steel (grey). Not shown are the cylindrical coils, that fit between the inner ledge of the yoke and the outside of the four pole pieces. The steel yoke quarters are 45 tons each, so these may need to be assembled from smaller parts.

When the "source terms" for these loss points are more completely understood, adequate shielding will be designed to satisfy the requirements for long and short term neutron control. These are standard procedures and we expect no difficulties.

3.3 Installation underground at Yemilab

The most challenging IsoDAR component for transport and installation will be the cyclotron. Basically, it is a cylindrical block with a diameter of 6 m, 2 m height, weighing 450 tons, but figure 26 gives an idea of its constituent parts. These parts are transported separately and assembled on site. The two particular challenges are the weight of the heaviest steel pieces of the cyclotron magnet, and the size of the magnet coils.

Commercial transport weight limits are around 50 tons per load, but the maximum weight for the magnet sections will be less than this, and will be set by the ability to move heavy weights in the underground caverns; in particular by the rigging capacity that will be available in the Cyclotron Room. The size of the steel for the magnet yoke and pole pieces can be adjusted to match this capacity, and a cost-benefit analysis must be performed. Machining costs increase with number of pieces and tolerances of faces that must be machined with precision — an optimal size for machining is about 45 tons. This is offset by the size and cost of crane or other rigging device that will be used for the precision assembly of the cyclotron pieces. Magnet steel pieces packed for shipping can be transported directly to the IsoDAR caverns underground. This is facilitated by the presence of a rail terminal within a few km of the mine entrance, and by the capabilities of the large mining trucks

2022 JINST 17 P09042

Figure 27. Photo of cyclotron coils built by Buckley Systems, Auckland NZ. These coils are 3.3 m diameter, ours are 4.95. The proportions are about the same as ours. Notice the person in lower right.

to bring shipping pallets, transloaded from rail cars, down the mine ramp and directly to staging locations in the IsoDAR area.

Although cyclotron coils only weigh about 1.2 tons each, they present a different challenge. Each of the two copper coils is a torus of 4.95 m outer radius, and a cross section of 25 cm radially by 20 cm height. Figure 27 is included to give a sense of the coil size and shape. These cyclotron coils are 3.3 m in diameter, smaller than our 4.95 m.

The nominal dimension of the mine ramp and Yemilab drifts is 5×5 m, so in principle the coils, oriented at a 45° angle should fit through these passages. However the mining trucks cannot be used for this, the shape of the bed does not allow for loading the coils in this fashion. A special trailer, or a custom fixture for a fork lift, will need to be designed that can hold a coil oriented at the proper angle, along the diagonal of the tunnel.

If it is not possible to transport the coils through the ramps, the coils will need to be either wound underground, or segmented into two halves. Both of these options are technically feasible but would increase cost. A segmented coil carries the requirement of splicing both ends of every turn to make a single continuous current path. This drives the electrical properties from the most efficient with several hundred turns, to a very high-current, low-voltage configuration required for a coil with no more than about 15 turns.

3.3.1 Installation sequence

The first pieces to be installed will be the large iron and concrete shielding wall, shown as the large green block in figure 5 at the end of the target hall. The total volume of this wall is about 200 cubic meters, and has a weight of over 1,200 tons. It will be important to ensure the rock at the lip of this cavern is properly reinforced to support this weight. It will need to be installed before the structure for the LSC is put in place, to allow rigging and installation of support structures from both sides. The design of this wall must ensure tight fits and minimize cracks, as neutrons are notorious for finding their way through even the narrowest spaces between blocks.

Next will be the cyclotron. Trucks will deliver components to the Staging Area shown in red at the bottom of the Entrance Ramp in figure 23. They will be offloaded by a fork lift, and moved to

2022 JINST 17 P09042

a location inside the Cyclotron Room where an overhead crane can perform the precision rigging needed for assembly of the cyclotron.

Following the cyclotron will be the target shielding and sleeve. As can be inferred from figure 12 this structure is made up of large blocks of special concrete and steel pieces that will be assembled using the overhead crane. The 20 cm diameter beam pipe running the length of this structure interfaces with the evacuated entrance beam line, and allows convenient insertion of the target torpedo from the back.

Then follow the beam line components, power supplies, and support equipment. The MEBT will be assembled last, as it crosses the entrance ramp and so blocks truck access to the area.

3.4 IsoDAR utilities

The utilities for IsoDAR (electricity, water and air) will be integrated with substations and distribution centers designed to service the needs of the whole laboratory.

3.4.1 Electric power delivery

The power requirement for IsoDAR is 3.5 MW. The proton beam carries 600 kW of power. The efficiency of the accelerating system (wall-plug to beam through the RF system) is about 50%, yielding 1.2 MW for the RF power alone. The remaining electricity is for powering the ion source, cyclotron- and transport magnets, vacuum and water pumps, instrumentation, and controls.

KEPCO (Korean Electric Power Corporation) is currently contracted to deliver 10 MW to the site. 7.5 MW is reserved for the use of the Handuk mine. Yemilab will require 2.5 MW in addition to the dedicated IsoDAR needs. To meet these IsoDAR needs the power system will have to be upgraded to a total of 13.5 MW.

3.4.2 Cooling water

The 3.5 MW of electrical power supplied produces 3.5 MW of heat which needs to be removed. This will be accomplished with cooling water. No cooling water was originally planned for Yemilab, air circulation was sufficient to handle the expected Laboratory heat load. Pumping cooled air into the main Laboratory may still be sufficient for the main body of Yemilab, but the IsoDAR heat load will require a surface-located, modestly-sized cooling tower (< 1000 ton), with water lines run up and down through the personnel shaft.

Two “Primary” cooling loops are required for IsoDAR: the electrical systems having “Low Conductivity” water (LCW); while the target loop is filled with heavy water, this being part of the neutron-producing system as well as being the target coolant. Both these primary loops have heat exchangers that transfer their heat to a single secondary loop, which is run through the cooling tower on the surface.

3.4.3 Air circulation

Air into the main Yemilab area is provided by ducts running from the surface, down the personnel shaft and along the Yemilab Access Ramp. It is released at selected end points in the Laboratory to ensure continuous airflow through the underground spaces. As air is forced in, pressure in these Laboratory areas will always be slightly positive.

2022 JINST 17 P09042

The IsoDAR areas should be maintained at a slightly negative pressure, so air would always be flowing into this area. This is accomplished by drawing air out of the area and ducting it to the surface. Air is replenished from the main Yemilab atmosphere, through the only portal entryway at the head of the IsoDAR entrance ramp.

4 Conclusion

This paper has reviewed the status of IsoDAR@Yemilab, demonstrating that feasible technical and infrastructure designs have been developed for all aspects of the experiment. This paper quotes and condenses the CDR [4], which was developed within the context of reaching preliminary approval at Yemilab so that cavern construction could move forward. These designs show that IsoDAR@Yemilab can be constructed, and perform beyond Standard Model searches that reach deeply into unexplored parameter space [5].

Acknowledgments

This work was supported by NSF grants PHY-1912764 and PHY-1626069, and the Heising-Simons Foundation. Winklehner was also supported by funding from the Bose Foundation. We gratefully acknowledge support for this work from the Korean Institute for Basic Sciences, Grant IBS-R016-D1.

References

[1] S.-H. Seo, *Neutrino Telescope at Yemilab, Korea*, arXiv:1903.05368.

[2] A. Bungau et al., *Proposal for an Electron Antineutrino Disappearance Search Using High-Rate ^{8}Li Production and Decay*, *Phys. Rev. Lett.* **109** (2012) 141802 [arXiv:1205.4419].

[3] J.M. Conrad, M.H. Shaevitz, I. Shimizu, J. Spitz, M. Toups and L. Winslow, *Precision $\bar{\nu}_e$-electron scattering measurements with IsoDAR to search for new physics*, *Phys. Rev. D* **89** (2014) 072010 [arXiv:1307.5081].

[4] J.R. Alonso et al., *IsoDAR@Yemilab: A Conceptual Design Report for the Deployment of the Isotope Decay-At-Rest Experiment in Korea's New Underground Laboratory, Yemilab*, arXiv:2110.10635.

[5] J. Alonso et al., *Neutrino physics opportunities with the IsoDAR source at Yemilab*, *Phys. Rev. D* **105** (2022) 052009 [arXiv:2111.09480].

[6] MiniBooNE collaboration, *Updated MiniBooNE neutrino oscillation results with increased data and new background studies*, *Phys. Rev. D* **103** (2021) 052002 [arXiv:2006.16883].

[7] MiniBooNE collaboration, *Improved Search for $\bar{\nu}_\mu \to \bar{\nu}_e$ Oscillations in the MiniBooNE Experiment*, *Phys. Rev. Lett.* **110** (2013) 161801 [arXiv:1303.2588].

[8] LSND collaboration, *Candidate events in a search for anti-muon-neutrino —> anti-electron-neutrino oscillations*, *Phys. Rev. Lett.* **75** (1995) 2650 [nucl-ex/9504002].

[9] LSND collaboration, *Evidence for anti-muon-neutrino —> anti-electron-neutrino oscillations from the LSND experiment at LAMPF*, *Phys. Rev. Lett.* **77** (1996) 3082 [nucl-ex/9605003].

[10] LSND collaboration, *Evidence for nu(mu) —> nu(e) neutrino oscillations from LSND*, *Phys. Rev. Lett.* **81** (1998) 1774 [nucl-ex/9709006].

2022 JINST 17 P09042

[11] C. Athanassopoulos, L.B. Auerbach, R.L. Burman, I. Cohen, D.O. Caldwell, B.D. Dieterle et al., *Evidence for neutrino oscillations from muon decay at rest*, *Physical Review C* **54** (1996) 2685.

[12] C. Athanassopoulos, L.B. Auerbach, R.L. Burman, D.O. Caldwell, E.D. Church, I. Cohen et al., *Results on $\nu_\mu \to \nu_e$ oscillations from pion decay in flight neutrinos*, *Physical Review C* **58** (1998) 2489.

[13] LSND collaboration, *Evidence for neutrino oscillations from the observation of $\bar{\nu}_e$ appearance in a $\bar{\nu}_\mu$ beam*, *Phys. Rev. D* **64** (2001) 112007 [hep-ex/0104049].

[14] G. Mention, M. Fechner, T. Lasserre, T.A. Mueller, D. Lhuillier, M. Cribier et al., *The Reactor Antineutrino Anomaly*, *Phys. Rev. D* **83** (2011) 073006 [arXiv:1101.2755].

[15] C. Giunti and M. Laveder, *Statistical Significance of the Gallium Anomaly*, *Phys. Rev. C* **83** (2011) 065504 [arXiv:1006.3244].

[16] V.V. Barinov et al., *Results from the Baksan Experiment on Sterile Transitions (BEST)*, *Phys. Rev. Lett.* **128** (2022) 232501 [arXiv:2109.11482].

[17] IceCube collaboration, *eV-Scale Sterile Neutrino Search Using Eight Years of Atmospheric Muon Neutrino Data from the IceCube Neutrino Observatory*, *Phys. Rev. Lett.* **125** (2020) 141801 [arXiv:2005.12942].

[18] ATLAS collaboration, *Measurement of the top quark mass in the $t\bar{t} \to$ dilepton channel from $\sqrt{s} = 8$ TeV ATLAS data*, *Phys. Lett. B* **761** (2016) 350 [arXiv:1606.02179].

[19] M.H. Moulai, *Light, Unstable Sterile Neutrinos: Phenomenology, a Search in the IceCube Experiment, and a Global Picture*, Ph.D. thesis, MIT, 2021. arXiv:2110.02351.

[20] M. Hostert, D. McKeen, M. Pospelov and N. Raj, *Probing dark sectors with neutron-shining-through-a-wall experiments*, in preparation.

[21] A. Adelmann et al., *Cost-effective Design Options for IsoDAR*, arXiv:1210.4454.

[22] L.H. Waites, J.R. Alonso, R. Barlow and J.M. Conrad, *What is the potential impact of the IsoDAR cyclotron on radioisotope production: a review*, *EJNMMI Radiopharm. Chem.* **5** (2020) 6.

[23] A. Bungau, J. Alonso, L. Bartoszek, J.M. Conrad, E. Dunton and M.H. Shaevitz, *The shielding design concept for the ISODAR neutrino target*, 2020 *JINST* **15** T07002 [arXiv:1909.08009].

[24] M. Abs et al., *IsoDAR@KamLAND: A Conceptual Design Report for the Technical Facility*, arXiv:1511.05130.

[25] D. Winklehner et al., *High intensity cyclotrons for neutrino physics*, *Nucl. Instrum. Meth. A* **907** (2018) 231 [arXiv:1807.03759].

[26] D. Winklehner, J.M. Conrad, J. Smolsky and L. Waites, *High-current H2+ beams from a filament-driven multicusp ion source*, *Rev. Sci. Instrum.* **92** (2021) 123301 [arXiv:2008.12292].

[27] D. Winklehner, R. Hamm, J. Alonso, J.M. Conrad and S. Axani, *Preliminary design of a RFQ direct injection scheme for the IsoDAR high intensity H_2^+ cyclotron*, *Rev. Sci. Instrum.* **87** (2015) 02B929.

[28] A. Bungau, J. Alonso, L. Bartoszek, J. Conrad, M. Shaevitz and J. Spitz, *Optimizing the ^{8}Li yield for the IsoDAR Neutrino Experiment*, 2019 *JINST* **14** P03001 [arXiv:1805.00410].

[29] D. Winklehner, J.M. Conrad, J. Smolksy, L.H. Waites and P. Weigel, *New Commissioning Results of the MIST-1 Ion Source*, in *Proceedings of the 2021 International Conference on Ion Sources*, TRIUMF, Canada, 20–24 September 2021 [slides: https://indico.cern.ch/event/1027296/contributions/4479729/attachments/2312022/3934761/ICIS21_MIST-1_Slides.pdf].

2022 JINST 17 P09042

[30] D. Winklehner, A. Adelmann, A. Gsell, T. Kaman and D. Campo, *Realistic simulations of a cyclotron spiral inflector within a particle-in-cell framework*, *Phys. Rev. Accel. Beams* **20** (2017) 124201 [arXiv:1612.09018]

[31] J.J. Yang, A. Adelmann, M. Humbel, M. Seidel and T.J. Zhang, *Beam Dynamics in High Intensity Cyclotrons Including Neighboring Bunch Effects: Model, Implementation and Application*, *Phys. Rev. ST Accel. Beams* **13** (2010) 064201 [arXiv:1003.0326].

[32] J. Stetson, S. Adam, M. Humbel, W. Joho and T. Stammbach, *The commissioning of PSI injector 2 for high intensity, high quality beams*, in *Proceedings of the 13th International Conference on Cyclotrons and their Applications*, Vancouver, BC, Canada, 6–10 July 1992, pp. 36–39.

[33] T. Stammbach, S. Adam, T. Blumer, D. George, A. Mezger, P.A. Schmelzbach et al., *The PSI 2 mA beam and future applications*, *AIP Conf. Proc.* **600** (2001) 423.

[34] D. Winklehner, J.M. Conrad, D. Schoen, M. Yampolskaya, A. Adelmann, S. Mayani et al., *Order-of-magnitude beam current improvement in compact cyclotrons*, *New J. Phys.* **24** (2022) 023038 [arXiv:2103.09352].

[35] M. Seidel, *Injection and Extraction in Cyclotrons* in *Proceedings of the CAS — CERN Accelerator School: Beam Injection, Extraction and Transfer*, Erice, Italy, 10–19 March 2017, CERN Yellow Reports: School Proceedings, B. Holzer ed., Vol. 5/2018, CERN-2018-008-SP, CERN, Geneva (2018).

[36] T. Rinckel, D. Baxter, J. Doskow, P. Sokol and T. Todd, *Target performance at the low energy neutron source*, *Phys. Procedia* **26** (2012) 168.

2022 JINST 17 P09042